






# Integrated microwave photonic true-time delay with interferometric delay enhancement based on Brillouin scattering and microring resonators

LUKE MCKAY,<sup>1,2</sup> MORITZ MERKLEIN,<sup>1,2,\*</sup> YANG LIU,<sup>1,2</sup>  ALEX CRAMER,<sup>3</sup> JORDAN MAKSYMOW,<sup>3</sup> ANDREW CHILTON,<sup>3</sup> KUNLUN YAN,<sup>4</sup> DUK-YONG CHOI,<sup>4</sup>  STEPHEN J. MADDEN,<sup>4</sup> RICHARD DESALVO,<sup>3</sup> AND BENJAMIN J. EGGLETON<sup>1,2</sup> 

<sup>1</sup>The University of Sydney Nano Institute (Sydney Nano), The University of Sydney, Sydney, NSW 2006, Australia

<sup>2</sup>Institute of Photonics and Optical Science (IPOS), School of Physics, The University of Sydney, Sydney, NSW 2006, Australia

<sup>3</sup>L3Harris Technologies, 2400 N.E. Palm Bay Rd, Palm Bay, FL 32905, USA

<sup>4</sup>Laser Physics Centre, The Australian National University, Canberra, ACT 0200, Australia

\*[moritz.merklein@sydney.edu.au](mailto:moritz.merklein@sydney.edu.au)

**Abstract:** True-time delays are important building blocks in modern radio frequency systems that can be implemented using integrated microwave photonics, enabling higher carrier frequencies, improved bandwidths, and a reduction in size, weight, and power. Stimulated Brillouin scattering (SBS) offers optically-induced continuously tunable delays and is thus ideal for applications that require programmable reconfiguration but previous approaches have been limited by large SBS gain requirements. Here, we overcome this limitation by using radio-frequency interferometry to enhance the Brillouin-induced delay applied to the optical sidebands that carry RF signals, while controlling the phase of the optical carrier with integrated silicon nitride microring resonators. We report a delay tunability over 600 ps exploiting an enhancement factor of 30, over a bandwidth of 1 GHz using less than 1 dB of Brillouin gain utilizing a photonic chip architecture based on Brillouin scattering and microring resonators.

© 2020 Optical Society of America under the terms of the [OSA Open Access Publishing Agreement](#)

## 1. Introduction

True-time delays (TTD) are critical radio frequency (RF) components for signal processing, radio over fibre, phased array antennas, and have applications in communications and satellites [1–3]. By applying uniform delays to all frequency components within a given bandwidth, so as to not induce any temporal distortion of the signal [4]; TTDs overcome the difficulties of beam squint in phased array antennas which is an issue with phase shifters. Phase shifters apply a fixed phase shift independent of frequency [4]. Phase shifters have applications in arrayed signal processors, microwave filters amongst others [5]. TTDs have been implemented using photonic and electronic principles [6]. Electronic approaches typically rely on RF systems which consist of multiple stages of electronic up-conversion, and down-conversion, with each step contributing non-negligible levels of phase and amplitude noise, which increases with rising frequency [3,7]. Traditional electronic approaches also lack low-loss methods for signal distribution [3,7] and can be bulky [6]. Microwave photonic methods which modulate the RF signal onto an optical carrier and use photonic components to delay the signal offers a promising solution to these problems [3,7–9]. Microwave photonics combines RF engineering with optoelectronics, enabling broad bandwidths, high carrier frequencies, immunity to electromagnetic interference, compatibility with fibre optic cable for low loss signal distribution [7,9], and hence offers a powerful solution for next-generation TTDs [10].

Typically, TTD schemes based on microwave photonics make use of separate carrier tuning (SCT) which circumvents the requirement of applying a dispersive phase slope spanning from the optical carrier to the edge of the sideband [11]. If SCT is not used, the dispersive phase slope needs to span several tens of GHz range and it is challenging to simultaneously achieve broad bandwidths and large delays. Instead, the group delay requirements can be drastically reduced by applying only a dispersive phase slope to the optical sideband frequencies that carry RF signals while the phase of the optical carrier is adjusted independently by applying a separate narrowband phase shift.

Integrating these microwave photonics approaches on to compact photonic integrated circuits brings further significant advantages in terms of a reduction in size, weight and power which is critical in many applications [12]. Improvements in performance are also anticipated due to increased stability and reduced interface loss between components. Integrated microwave photonic TTDs have been demonstrated using a wide array of different methods including Bragg gratings [13], P-N junctions [14], photonic crystals [15], ring resonators [16–18], on-chip switched delay lines [19] and integrated optical comb sources [20,21]. Although impressive, these demonstrations have not shown simultaneous reconfigurability of the bandwidth and carrier frequency while maintaining a large delay bandwidth product.

Stimulated Brillouin scattering (SBS), a nonlinear optical effect, can induce a narrowband phase shift [22,23] as well as a broadband group delay [24–27], and can be integrated on a chip [28,29]. SBS based true-time delays offer flexibility to rapidly and continuously adjust bandwidth, carrier frequency, and delay with a high spectral resolution, making SBS ideal for applications where rapid adjustments are required for dynamic RF environments [30,31]. However, the main limitation of on-chip TTD using Brillouin scattering and SCT has been the high SBS gain and associated power requirements that has limited the achievable delay and phase shift. Even for record levels of on-chip Brillouin gain (52dB), the delay and the corresponding phase shift was limited to 200° [32].

In this work, we overcome these limitations by combining on-chip SBS with on-chip silicon nitride (SiN) microring resonators and RF interferometric delay enhancement. The SiN microring resonator is used to induce a phase shift on the optical carrier while we utilize on-chip SBS to apply a broadband tunable delay to the sideband, which is further enhanced by RF interferometry. We experimentally show a microwave TTD system with a delay of 600 ps over a bandwidth of 1 GHz using less than 1 dB of Brillouin gain distributed over the signal bandwidth; this corresponds to an enhancement of 30 times from an initial delay of 20 ps. On-chip ring resonators enable 360° phase tunability in a SiN platform. We give a roadmap toward integrating the whole system on a single chip.

## 2. Principle

The basic principle of the presented TTD is shown in Fig. 1. An input signal  $RF_{in}$  (Fig. 1(a)) is modulated on the optical carrier (C) which results in optical sidebands (SB) (Fig. 1(b)). Our TTD (Fig. 1(blue box)) is achieved by harnessing three elements: A broadband delay applied to the sideband (Fig. 1(c)), an interferometric delay enhancement (Fig. 1(d)) to increase the overall delay, and a phase shifter (Fig. 1(e)) that controls the phase of the optical carriers. For an MWP TTD with a single sideband modulated signal, the delay of a dispersive phase slope spanning from the optical carrier through the sideband  $T_d$  is given as:

$$T_d = \frac{\delta\Phi_k}{\delta f} \Big|_{f_{SB}-f_c} \quad (1)$$

$\Phi_k$  is the phase,  $f_c$  is the frequency of the RF carrier,  $f_{SB}$  is the frequency of the RF sideband. Using separate carrier tuning [11] the dispersive phase slope is only required over the sideband.

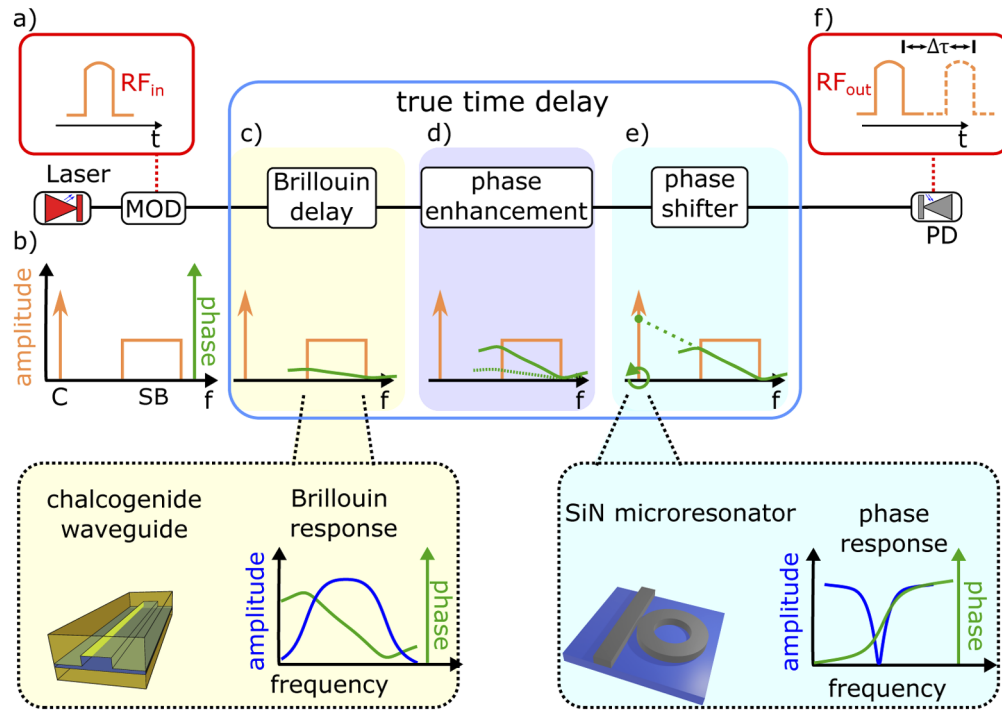


**Fig. 1.** Block diagram of the true time delay. a) RF input signal and b) corresponding optical spectrum. The input signal  $RF_{in}$  (orange) is modulated on an optical signal resulting in a carrier (C) and a sideband (SB). The true-time delay element (blue box) consists of three elements, c) the Brillouin group delay applied to the sideband using a chalcogenide waveguide (inset shows the chalcogenide waveguide and SBS profile), d) interferometric delay enhancement and e) a phase shifter implemented using thermally controlled SiN ring resonator (inset shows the microring resonator as well as the phase and amplitude response). f) The optical signal is converted back to the RF domain using a photodetector (PD) leading an RF signal  $RF_{out}$  delayed by  $\Delta\tau$  (dotted orange line).

The group delay over the sideband is initially achieved with SBS (Fig. 1(c)), which was chosen due to its tunability of both bandwidth and frequency and its ability to induce gain-based group delays [26,27,33,34]. The broadband Brillouin gain was applied by multiple equally spaced counter-propagating optical pumps. The phase response of the pumps sum together to result in a linear broadband dispersive phase slope applied to the optical sideband [24,25]. The Brillouin induced group delay was then enhanced using an RF interferometric approach (Fig. 1(d)).

Interferometry is capable of amplifying phase shifts, which in turn amplifies the corresponding group delay when applied to the sideband. Multiple interferometric enhancement schemes have been demonstrated previously [35–38]. These approaches rely upon generating an additional RF signal which destructively interferes with the initial RF signal, leading to the delay enhanced output.

When the dispersive phase slope is only applied to the sideband a corresponding phase shift is then applied to the optical carrier to prevent temporal distortions of the signal envelope. The phase shift on the carrier is given in terms of delay ( $T_{RF}$ ) where:

$$T_{RF} = \frac{\Phi_k(f_c + f_{SB}, t) - \Phi_k(f_c, t)}{f_{SB}} \quad (2)$$

The phase shift is applied to the optical carrier with a thermally controlled microring resonator integrated on a SiN chip (Fig. 1(e)). There are many ways to implement optical phase shifts but microring resonators are very suitable as they are wavelength selective and are easily controllable with heaters [39,40]. To achieve arbitrary phase shifts using SBS, it would require prohibitively high levels of gain, more than 50 dB [41]. Microring resonators can be implemented in chalcogenide [42] or in a hybrid silicon and chalcogenide platform, enabling high levels of Brillouin gain with the flexibility of silicon photonic integrated circuits [43]. Silicon nitride was chosen due to its low propagation loss, leading to high Q resonators [44] and ease of integration with other materials [45].

To meet the SCT condition and generate a true-time delay ( $T_{TTD}$ ), the following condition must be met:

$$T_{TTD} = T_d = T_{RF} \quad (3)$$

The optical tones then beat at the photodetector (PD) and generate the delayed signal (dotted orange line)  $RF_{out}$  (Fig. 1(f)).

The principle behind the delay enhancement process can be seen in Fig. 2. In order to highlight the concept, initially, the monotone case will be considered. To enable the delay enhancement, the interference condition needs to be configured. To achieve this both optical carriers ( $C_1$  and  $C_2$ ) are passed through the phase modulator and opposing sidebands are removed, leaving monotone sidebands  $SB_1$  and  $SB_2$ , shown in Fig. 2(a). SBS is applied to  $SB_1$ , which induces a gain based phase shift. The spectral separation of  $C_2$  and  $C_1$  is higher than the cut off response frequency.  $SB_2$  and  $C_2$  beat at the PD and generate the RF tone  $RF_{int}$ . Correspondingly,  $SB_1$  and  $C_1$  beat to generate  $RF_{SBS}$ . Both vectors destructively interfere and result in  $RF_{net}$ . This is depicted in Fig. 2(b) in the complex plane. The complex plane is a powerful tool for visualizing the dispersive group delay and interferometric enhancement in the RF domain. A vector spanning from the origin to a point on the complex plane has its magnitude given by its length and the phase of the RF signal is given by the angle of the vector. The phasors  $RF_{SBS}$  and  $RF_{int}$  interfere and through vector addition and result in the new phasor  $RF_{net}$ . The phase of  $RF_{net}$  is larger than the phase of  $RF_{SBS}$ , which is shown in Fig. 2(c).

To extend the concept above to a practical TTD, the narrowband sidebands are replaced with broadband signals. Broadband Brillouin gain is applied to  $SB_1$  as shown in Fig. 2(d). The broadband Brillouin response consists of the sum of multiple spectrally separated narrowband Brillouin responses. The Brillouin amplitude and phase response are modeled in [34,41]. The broadband amplitude response is given by  $A(f)$ , the corresponding phase shift is given by  $\theta_{SBS}(f)$ , the phase offset applied by the microring resonator is given as  $\theta_1$  and  $f$  is frequency. After detection, the resultant range of RF signals can be expressed by :

$$RF_{SBS}(f) = A(f) \exp(i(\theta_{SBS}(f) + \theta_1)) \quad (4)$$

$RF_{SBS}$  consists of a family of vectors in the complex plane, depicted as a curve as each frequency component of the optical sideband has a unique phase applied to it (Fig. 2(e)).

The amplitude of the interference signal is given as  $B_{int}$  and has a corresponding phase of  $\theta_2$ . The vector  $RF_{int}$  is then defined as:

$$RF_{int} = B_{int} \exp(i\theta_2) \quad (5)$$

$RF_{SBS}$  interferes with  $RF_{int}$  and results in the new vector family response  $RF_{net}$ . The enhanced output  $RF_{net}$  is then given as:

$$RF_{net}(f) = A(f) \exp(i(\theta_{SBS}(f) + \theta_1)) + B_{int} \exp(i\theta_2) \quad (6)$$

The curve traced by  $RF_{net}$  lies closer to the origin and therefore the vectors comprising it have a greater phase range than  $RF_{SBS}$ . The interference component  $RF_{int}$  is required to have a

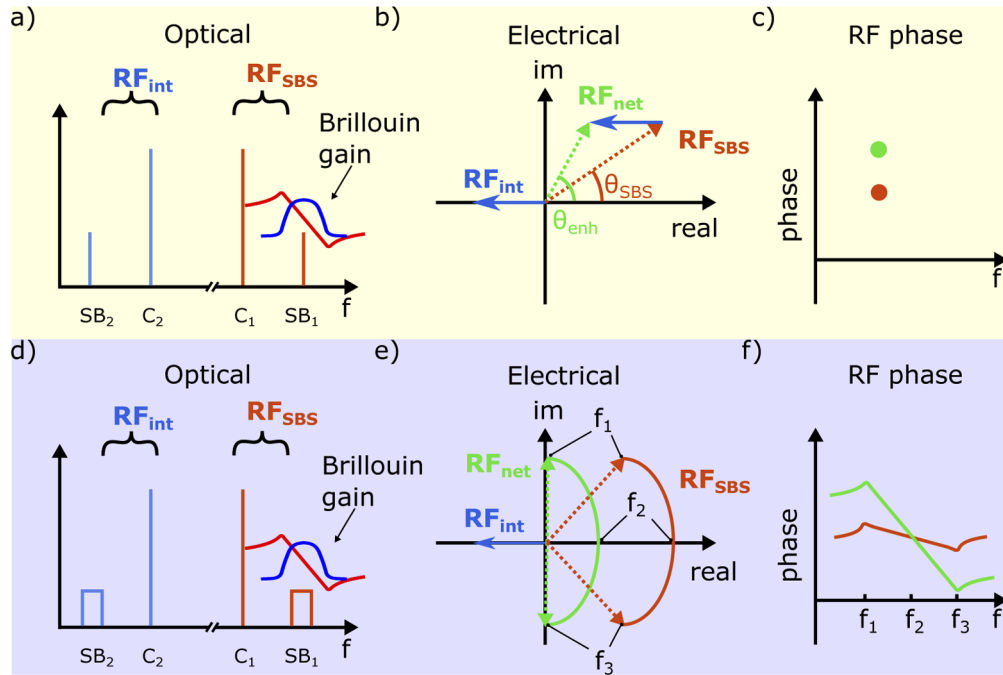


**Fig. 2.** A monotone signal is used to highlight the principle of the TTD. The monotone optical signals are configured in a) to generate two out of phase RF tones  $\mathbf{RF}_{SBS}$  and  $\mathbf{RF}_{int}$  shown in b). SBS applies a phase shift ( $\theta_{SBS}$ ) to the phasor  $\mathbf{RF}_{SBS}$  and destructively interferes with  $\mathbf{RF}_{int}$  to generate the phase enhanced resultant  $\mathbf{RF}_{net}$  with phase  $\theta_{enh}$  (c). d) The optical signals are configured to operate in the broadband regime and SBS is applied over the upper sideband which leads to a broadband family of vectors  $\mathbf{RF}_{SBS}$  in e). The vectors in  $\mathbf{RF}_{SBS}$  interfere with  $\mathbf{RF}_{int}$  and the resultant vector family encompasses a larger range of phases and hence a greater delay. The corresponding phase slopes are plotted in f).

$180^\circ$  phase offset from  $\theta_{SBS}(0)$ , which has a value of  $0^\circ$  if no other phase shifts have been applied ( $\theta_1 = 0$ ), for this to be true  $\theta_2 = 180^\circ$ . The corresponding phase slope of  $\mathbf{RF}_{net}$  is larger than the slope of  $\mathbf{RF}_{SBS}$ , so induces a larger group delay representing the delay enhancement (Fig. 2(f)).

To apply a phase shift to meet the SCT condition, both optical carriers need to be rotated the same direction around the complex plane, while remaining  $180^\circ$  out of phase with one another. If this condition is not met, the interference condition will also no longer be met and the delay of  $\mathbf{RF}_{net}$  will be distorted. The phase of  $\theta_1$  and  $\theta_2$  are applied by applying optical phase shifts to  $C_1$  and  $C_2$ , respectively. However, as the sidebands are on the opposing sides of their respective carrier, the sign of the phase shifts applied to  $C_1$  and  $C_2$  need to be in opposing directions to ensure  $\theta_1$  and  $\theta_2$  rotate in the same direction.

The delay enhancement factor  $G$  is a scalar value which gives the enhanced delay when multiplied by the delay of the unenhanced broadband Brillouin response. The delay is related to the derivative of the dispersive phase slope, so  $G$  can be calculated with the following equation:

$$G = \frac{\theta_{enh}(f_{max}) - \theta_{enh}(f_{min})}{\theta_{SBS}(f_{max}) - \theta_{SBS}(f_{min})} \quad (7)$$

The frequencies  $f_{max}$  and  $f_{min}$  correspond to the maximum and minimum phase shifts in the unenhanced Brillouin response.  $\theta_{enh}$  is the enhanced broadband phase profile is given by:

$$\theta_{enh}(f) = \arctan\left(\frac{A(f)\sin(\theta_{SBS}(f))}{A(f)\cos(\theta_{SBS}(f)) - B_{int}}\right) \quad (8)$$



As it can be seen in equation Eq. 8 the enhancement can be controlled by varying the amplitude of the interference component  $B_{\text{int}}$ .

The TTD presented here shares some similarities with the work presented in [38]. Both schemes utilize RF interferometric phase enhancement of a backward SBS signal with the main difference that the Brillouin gain in this work is applied to the sideband and a microring resonator is used for phase control to meet the separate carrier tuning condition, whereas Brillouin gain is only applied to the carrier in [38]. The phase shifter presented in [38] has a fixed enhancement factor for a give amount of Brillouin gain, while in the case of the TTD enhancement factor is used to control the delay. The work [38] explores the reduction in link gain and the associated link variation with different phase enhancement factors. This aspect of the analysis also applies in the case of the TTD. For the 1GHz measurement, there was a maximum link variation of 15 dB between the smallest and largest measured phase enhancement factors.

The TTD has an inherent trade-off between bandwidth and link gain. If the pump consists of more comb lines to facilitate a broader bandwidth, the amplitude of each line is reduced. This results in a shallower dispersive phase slope over the bandwidth which must be compensated for with a larger phase enhancement factor. The increased phase enhancement factor reduces link gain and is more sensitive to phase errors between the interferometric components, as analysed in [38].

### 3. Experimental setup

The experimental setup is shown in Fig. 3. The optical tone from laser 1 ( $C_1$ ) is split into two paths, the pump and signal paths. The upper path generates the pump, the signal from the laser passes through a dual-parallel Mach Zehnder modulator (DPMZM) driven by an arbitrary waveform generator (AWG). The DPMZM is biased to consist of only the upper sideband, with both the optical carrier and lower sideband suppressed. The output is amplified with an erbium doped fibre amplifier (EDFA) and any spurious components are removed using a bandpass filter (BPF). The signal continues to pass through a circulator before coupling into the chalcogenide waveguide. The chalcogenide rib waveguide was made out of  $\text{As}_2\text{S}_3$  [46] with a width of  $2.4 \mu\text{m}$ , a height of 950 nm, an etch depth of 320 nm, and was 23 cm long. There was a coupling loss of 4 dB per facet, with a total insertion loss of 19.1 dB. The AWG produced 50 equally spaced tones 20 MHz apart for a total bandwidth of 1 GHz. Each of the tones generated by the AWG had an approximately constant amplitude. The tones generated by the AWG were spectrally offset 7.8 GHz higher than the RF sideband, a frequency equal to the Brillouin frequency shift. The signal was then amplified before being sent into the DPMZM. Throughout all the measurements, the optical pump had a combined power of 24 dBm, except for the 450 MHz bandwidth experiment which had 24.4 dBm pump power. For the 450MHz measurement the pump profile consisted of 25 lines with 20 MHz separation and equal amplitude leading to a bandwidth of 500MHz. The edges of the 500MHz wide profile were discarded due to distortion.

The signal path branching from laser 1 passes through a phase modulator. The RF signal from the vector network analyzer (VNA) modulates the optical carrier before coupling into the chalcogenide waveguide. The upper sideband experiences Brillouin gain from the pump before continuing through a BPF which removes the pump back reflection. The signal is amplified by a low noise EDFA before it continues through a dual bandpass filter where the lower sideband is removed leaving  $C_1$  and  $\text{SB}_1$ . A tunable phase shifter (TPS) then acts on  $C_1$ . The purpose of the TPS is to ensure that the phase of both RF vectors are  $180^\circ$  out of phase. The TPS is implemented with thermally controlled microring resonators in a separate SiN chip, with an insertion loss of 9.3 dB. The optical power in the microring resonators was not high enough to induce any noticeable thermal drift as low signal powers were used and the Brillouin pump back reflection from the chalcogenide chip was removed. Additionally, the microrings used were located on opposing sides of the optical chip to reduce thermal crosstalk. The rings were also configured

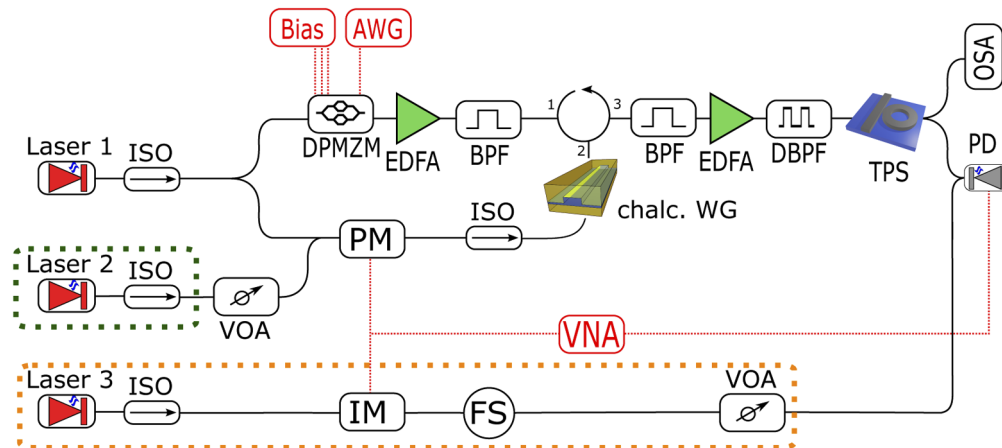


**Fig. 3.** Experimental layout of the TTD with the two-tap filter shown in the orange box. The delay enhancement is controlled with laser 2 (shown in green). AWG, arbitrary waveform generator; BPF, band-pass filter; DBPF, dual band-pass filter; FS, fibre spool; TPS, tunable phase shifter; chalc. WG, chalcogenide waveguide; OSA, optical spectrum analyser; PM, phase modulator; ISO, isolator; EDFA, erbium doped fibre amplifier; DPMZM, dual-parallel Mach Zehnder modulator; VOA, variable optical attenuator; IM, intensity modulator; PD, photodetector; Bias, modulator bias voltages; VNA, vector network analyzer.

to operate in a shallow over-coupled regime to reduce sensitivity to drift. The stability of the TTD could be improved further by implementing a feedback mechanism in the TPS to ensure the interferometric components are  $180^\circ$  out of phase. The signal beats on the PD and generates the delayed signal  $\mathbf{RF}_{\text{SBS}}$  which was recorded on the VNA. The optical spectrum is characterized by an optical spectrum analyzer that was connected to the 10% port of a 90:10 splitter after the TPS.

To enhance the delay, a second optical source is generated from laser 2 ( $C_2$ , shown in green). Laser 2 (193.347 THz) is set to a lower frequency than laser 1 (193.402 THz), spectrally separated to ensure there was no beating between the two lasers at the detector. The signal from laser 2 is fed through a variable optical attenuator (VOA) before passing through the phase modulator. The second optical carrier also passes through the chalcogenide waveguide, however, it does not experience any Brillouin gain. The signal continues through the BPF and DBPF where the upper sideband is removed leaving  $C_2$  and  $SB_2$ . A second ring from the TPS induces an optical phase shift on  $C_2$  before  $C_2$  and  $SB_2$  beat together at the PD generating the signal  $\mathbf{RF}_{\text{int}}$ .

In order to characterise the TTD performance, we implemented a two-tap filter (TTF) by adding a third laser, the TTF compares a known delay to that of the TTD. The optical signal from the laser was fed through an intensity modulator (IM) which is driven by the VNA, so the IM has an identical RF input as the PM. This signal propagates through a spool of single-mode fibre (FS) before passing through a VOA and beating on the PD. The VOA is used to control the amount of destructive RF interference of the TTF at the PD, additionally, the VOA also acts as a switch to turn the TTF off entirely.

#### 4. Results

The key functionality of the TTD is demonstrated in this section. The enhanced dispersive phase slope and corresponding delay are shown over a bandwidth of 1 GHz and again at 450 MHz to highlight the programmable reconfigurability with a near constant delay bandwidth product. A  $360^\circ$  continuously tunable phase shift is also demonstrated to ensure the SCT condition can always be met for any given delay or carrier frequency. Finally, the experimental results are

verified with a two-tap filter which experimentally confirms both continuous phase tunability and a change in group delay.

Initially, laser 1 was used to generate an un-enhanced group delay with SBS. The optical pump had a combined power of 24 dBm over the 1 GHz bandwidth. The pump produced a delay of 20 ps and less than 1 dB of broadband Brillouin gain, which can be seen in Fig. 4(a)). The second interference laser was then added and with the same amount of pump power resulted in 600 ps of delay tunability which represents an enhancement factor of 30. Delay tunability here is defined as the maximum range of group delay and advancement.

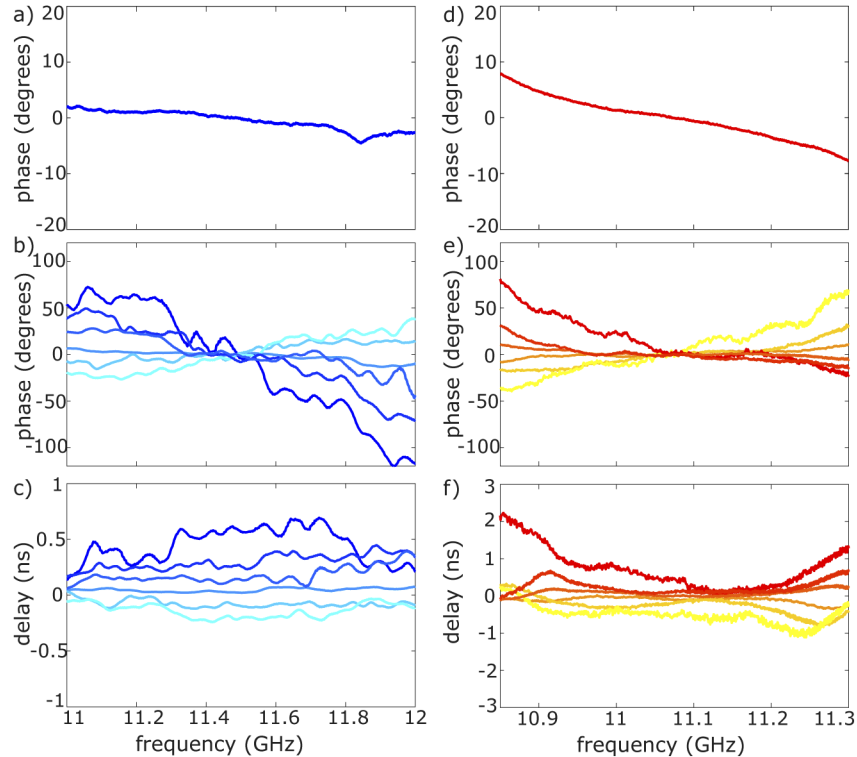


**Fig. 4.** Experimental results highlight the delay enhancement, broad bandwidths and reconfigurable properties of the proposed TTD. The left column demonstrates a 1 GHz bandwidth while the right column shows a 450 MHz bandwidth. a) Unenhanced Brillouin phase profile over 1 GHz bandwidth. b) Dispersive phase slope measurements with a delay enhancement tuning range of 30 over 1 GHz bandwidth. c) Corresponding delay measurements with a rolling average filter applied. d) Unenhanced Brillouin phase profile over 450 MHz bandwidth. e) Dispersive phase slope measurements with a delay enhancement range of 13.5 over 450 MHz bandwidth. f) Corresponding delay measurements with a rolling average filter applied.

Changing the intensity of  $\mathbf{RF}_{\text{int}}$  with the VOA affects the enhancement, which in turn controls the delay. The TPS was used to ensure the RF vectors were  $180^\circ$  out of phase with each other. The variable delays can be seen in Fig. 4(b)). The resultant dispersive phase slope is continuously tunable and can be significantly steeper than the unenhanced case. Additionally, it is also possible to invert the sign of the dispersive phase slope when  $\mathbf{RF}_{\text{int}}$  is large (see equation 6). When  $\mathbf{RF}_{\text{int}}$  is larger than  $\mathbf{RF}_{\text{SBS}}$ , the resultant vector  $\mathbf{RF}_{\text{net}}$  sits on the opposing side of the origin on the complex plane, so the sign of the slope is inverted. Each dispersive phase slope in Fig. 4(b)) has a corresponding delay plotted in the same colour in Fig. 4(c)). The fluctuations present in



Fig. 4(a) are amplified by the enhancement factor present in Fig. 4(b)). The delay was calculated by finding the average dispersive phase slope over the signal bandwidth. The delay fluctuations could be improved with further phase and amplitude engineering. In this experiment there are two main sources of distortion in the delay. One is the non-uniformity of the Brillouin gain profile. Ripples present in the unenhanced phase profile will be amplified by the phase-enhancement. A second source of distortion is the potential misalignment of the interfering vectors. This occurs when  $\theta_1$  is not  $180^\circ$  out of phase of  $\theta_2$  and can result in deterministic phase errors. These fluctuations could be reduced further by implementing a feedback mechanism to control the amplitude of the various optical pump tones to tailor the shape of the Brillouin phase response before the delay enhancement is applied. Additionally, the delay plotted in Fig. 4(c) is related to the derivative of the dispersive phase slope in b), which further highlighted distortion. The delay bandwidth-product was measured to be 0.6.

The experiment was repeated over a bandwidth of 450 MHz to highlight the bandwidth tunability of the TTD. 24.4 dBm of optical pump power was used over the signal bandwidth, resulting in around 1 dB of broadband Brillouin gain. This generated a dispersive phase slope plotted in Fig. 4(d)), which had a calculated delay of 93 ps. The distortion in the delay profile is due to a phase error between the interfering components. This issue could be alleviated with a feedback mechanism implemented with the TPS to ensure the interferometric components are correctly aligned, with phase separation of  $180^\circ$ . The interference laser was configured in Fig. 4(e) and a delay enhancement factor of 13.5 was demonstrated, representing a delay tunability of 1.27 ns and a delay-bandwidth product of 0.57, shown in Fig. 4(f)). To demonstrate continuous phase control to ensure SCT can always be met, the phase of the optical carriers were tuned with the SiN microring resonators while a constant group delay was applied. The enhancement was achieved using a constant pump power of 24 dBm used over a bandwidth of 1 GHz. The enhancement laser was then configured, leading to a delay of 100 ps, which represents a delay enhancement factor of 5. The phase of the optical carriers was then rotated as shown in Fig. 5. The phase is tunable over a range of  $360^\circ$  so it is possible to always meet the SCT condition from any carrier frequency or delay. The link gain would ideally remain constant

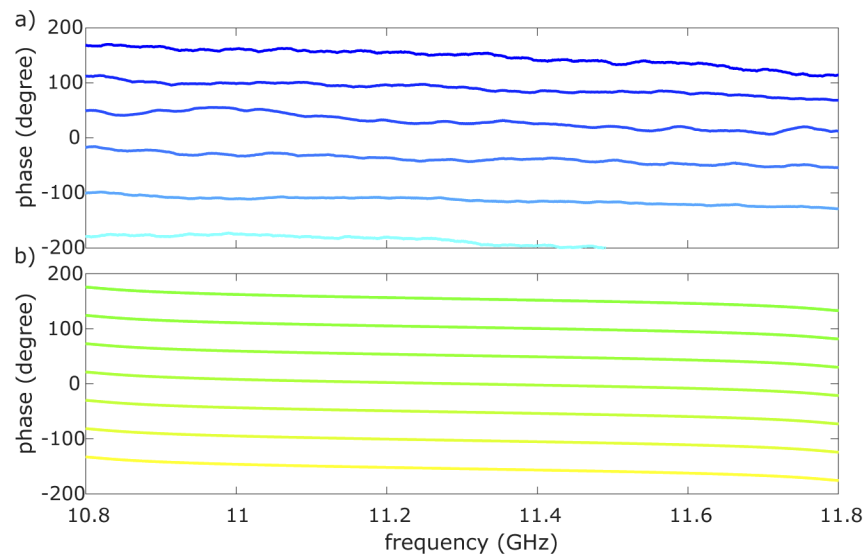


**Fig. 5.** A phase shift was applied to the optical carriers of the TTD with a delay enhancement factor of 5, providing arbitrary  $360^\circ$  phase control. a) experimental results, b) theoretical model from equation 6.

as the interference condition has remained constant, however, the link deviated by 7.6 dB over a  $360^\circ$  phase shift caused by the loss resonance of the microring resonators. This loss could be reduced by further optimizing the microring resonator, or as the loss is deterministic it could be corrected for with a variable-gain amplifier.

A two-tap filter was used to characterize the response of the TTD, shown in the orange box in Fig. 3. A two-tap filter consists of an optical signal which is encoded with the same RF information as the TTD. The TTF signal runs parallel to TTD and beats on the same photodetector but with an engineered path-length mismatch. The pathlength of the TTF was controlled by passing it through a fibre spool. This is to facilitate an appropriate free spectral range such that only a few local minima are in the bandwidth over which the delay is applied. The RF signal from the TTF interferes with the broadband signal  $\mathbf{RF}_{\text{net}}$  and results in an interference pattern. The free spectral range of the interference pattern is determined by the difference in the time delay between the interference arm and the true-time delay. This makes it possible to measure the induced delay [30]. Additionally, the phase difference between the two RF signals can be determined from the spectral location of the minima, which can be used to confirm that the SCT condition has been met. The phase of the optical carriers were rotated by  $360^\circ$  and the corresponding interference pattern was plotted in Fig. 6(a)). Here, the spectral location of the minima can be moved to arbitrary locations without altering the FSR, which demonstrates  $360^\circ$  phase tunability. Similarly, the delay can also be measured with the two-tap filter. When the pump is off, the interference pattern is plotted in orange in Fig. 6(b)). The pump is then turned on, inducing a 330 ps change in the delay of the TTD and can be seen by a change of approximately 20 MHz in the free spectral range of the interference pattern. The minima in the figure have been shifted so they align, to better emphasize the change in FSR.

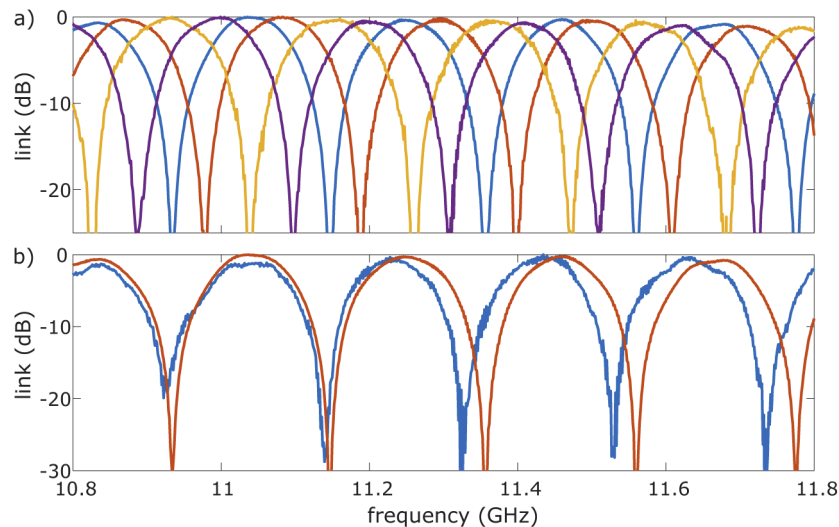


**Fig. 6.** Two-tap filter results: a) A phase shift was applied to the two optical carriers that shift the interference minima, here we show arbitrary  $360^\circ$  phase tunability. b) A delay was applied which induced a change in the free spectral range of the interference pattern. Orange - filter response when the pump is off. Blue interference pattern when the pump was turned on.

## 5. Conclusion and outlook

In this paper, we have demonstrated an integrated true-time delay based on an on-chip architecture that combines SBS and, RF interference and integrated silicon nitride microring resonators. We have demonstrated continuously tunable delays using very low levels of on-chip Brillouin gain, while simultaneously showing arbitrary  $360^\circ$  on-chip phase tuning with silicon nitride microring resonators. The true-time delay configuration lends itself to future integration, where all the components could be integrated into a single hybrid chip, as illustrated in the artist's impression of the chip shown in Fig. 7. Integration would reduce the size, weight and power (SWaP) of the system and increase the stability due to more constant optical path lengths. Integration would also significantly reduce loss associated with the interface between components, which was a large source of loss in the experiments performed in this manuscript. Integrating the chalcogenide into a hybrid chip would remove the need for a pump back reflection filter due to the high degree of mode matching between silicon and chalcogenide, which has insignificant back reflections [43].

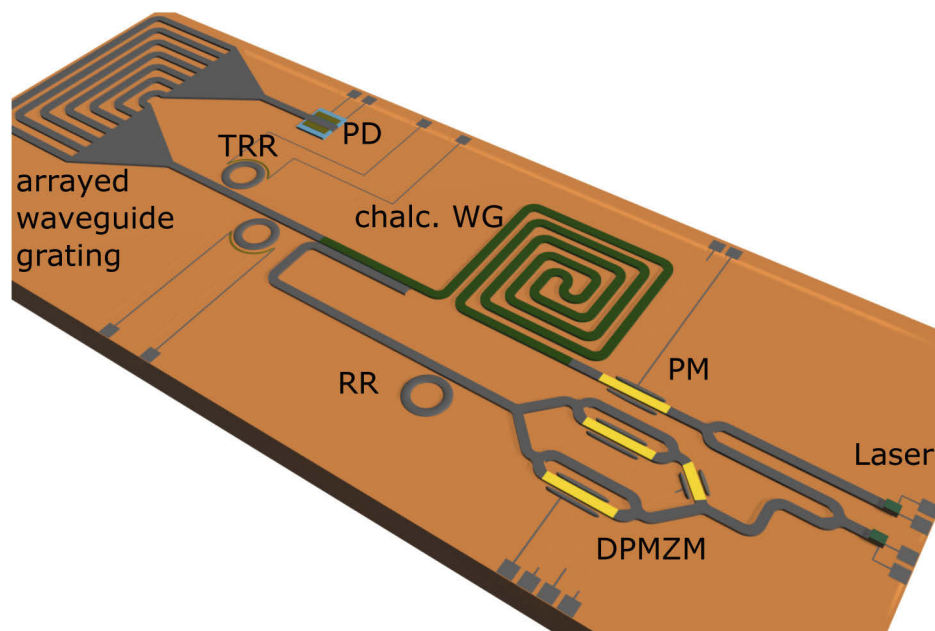


**Fig. 7.** Artists impression of a fully integrated SBS microwave photonic true-time delay. TRR, tunable ring resonator; PD, photodetector; DPMZM, dual-parallel Mach Zehnder modulator; chalc. WG, chalcogenide waveguide; PM, phase modulator.

As silicon waveguide losses are improved [47], it is foreseeable that the microring resonators could be implemented in silicon directly without needing to incorporate silicon nitride into the same chip. The chalcogenide platform could potentially be replaced with a silicon structure which enable forward Brillouin scattering [48,49]. Constructing the TTD from a single optical material would reduce complexity and streamline the fabrication process. Additionally, phonon coupling between adjacent waveguides could be used so an optical filter to remove the Brillouin pump would no longer be required [50].

## Funding

Office of Naval Research Global (N62909-18-1-2013); U.S. Air Force (FA2386-16-1-4036); Australian Research Council (LP170100112).

## Acknowledgments

This work was performed in part at the ACT node of the Australian National Fabrication Facility, a company established under the National Collaborative Research Infrastructure Strategy to provide nano- and micro-fabrication facilities for Australia's researchers.

## Disclosures

The authors declare no conflicts of interest.

## References

1. W. Ng, A. A. Walston, G. L. Tansonan, J. J. Lee, I. L. Newberg, and N. Bernstein, "The first demonstration of an optically steered microwave phased array antenna using true-time-delay," *J. Lightwave Technol.* **9**(9), 1124–1131 (1991).
2. I. Frigyes and A. J. Seeds, "Optically generated true-time delay in phased-array antennas," *IEEE Trans. Microwave Theory Tech.* **43**(9), 2378–2386 (1995).
3. J. Yao, "Microwave photonics," *J. Lightwave Technol.* **27**(3), 314–335 (2009).
4. R. Rotman, M. Tur, and L. Yaron, "True time delay in phased arrays," *Proc. IEEE* **104**(3), 504–518 (2016).
5. R. Maram, S. Kaushal, J. Aza na, and L. Chen, "Recent trends and advances of silicon-based integrated microwave photonics," *Photonics* **6**(1), 13 (2019).
6. M. Longbrake, "True time-delay beamsteering for radar," in *2012 IEEE National Aerospace and Electronics Conference (NAECON)*, (2012), pp. 246–249.
7. G. Serafino, F. Scotti, L. Lembo, B. Hussain, C. Porzi, A. Malacarne, S. Maresca, D. Onori, P. Ghelfi, and A. Bogoni, "Toward a new generation of radar systems based on microwave photonic technologies," *J. Lightwave Technol.* **37**(2), 643–650 (2019).
8. A. J. Seeds and K. J. Williams, "Microwave photonics," *J. Lightwave Technol.* **24**(12), 4628–4641 (2006).
9. J. Capmany and D. Novak, "Microwave photonics combines two worlds," *Nat. Photonics* **1**(6), 319–330 (2007).
10. J. Capmany, J. Mora, I. Gasulla, J. Sancho, J. Lloret, and S. Sales, "Microwave photonic signal processing," *J. Lightwave Technol.* **31**(4), 571–586 (2013).
11. P. A. Morton and J. B. Khurgin, "Microwave photonic delay line with separate tuning of the optical carrier," *IEEE Photonics Technol. Lett.* **21**(22), 1686–1688 (2009).
12. D. Marpaung, "Integrated microwave photonics," *Nat. Photonics* **13**(2), 80–90 (2019).
13. M. Burla, L. R. Cortés, M. Li, X. Wang, L. Chrostowski, and J. Azaña, "On-chip programmable ultra-wideband microwave photonic phase shifter and true time delay unit," *Opt. Lett.* **39**(21), 6181–6184 (2014).
14. W. Zhang and J. Yao, "Invited article: Electrically tunable silicon-based on-chip microdisk resonator for integrated microwave photonic applications," *APL Photonics* **1**(8), 080801 (2016).
15. C.-J. Chung, X. Xu, G. Wang, Z. Pan, and R. T. Chen, "On-chip optical true time delay lines featuring one-dimensional fishbone photonic crystal waveguide," *Appl. Phys. Lett.* **112**(7), 071104 (2018).
16. X. Wang, L. Zhou, R. Li, J. Xie, L. Lu, K. Wu, and J. Chen, "Continuously tunable ultra-thin silicon waveguide optical delay line," *Optica* **4**(5), 507–515 (2017).
17. M. Burla, D. A. I. Marpaung, L. Zhuang, M. R. Khan, A. Leinse, W. Beeker, M. Hoekman, R. G. Heideman, and C. G. H. Roeloffzen, "Multiwavelength-integrated optical beamformer based on wavelength division multiplexing for 2-d phased array antennas," *J. Lightwave Technol.* **32**(20), 3509–3520 (2014).
18. L. Zhuang, C. G. H. Roeloffzen, A. Meijerink, M. Burla, D. A. I. Marpaung, A. Leinse, M. Hoekman, R. G. Heideman, and W. van Etten, "Novel ring resonator-based integrated photonic beamformer for broadband phased array receive antennas—part ii: Experimental prototype," *J. Lightwave Technol.* **28**(1), 19–31 (2010).
19. J. Xie, L. Zhou, Z. Li, J. Wang, and J. Chen, "Seven-bit reconfigurable optical true time delay line based on silicon integration," *Opt. Express* **22**(19), 22707–22715 (2014).
20. X. Xu, J. Wu, T. G. Nguyen, T. Moein, S. T. Chu, B. E. Little, R. Morandotti, A. Mitchell, and D. J. Moss, "Photonic microwave true time delays for phased array antennas using a 49 GHz FSR integrated optical micro-comb source," *Photonics Res.* **6**(5), B30–B36 (2018).
21. X. Xue, Y. Xuan, C. Bao, S. Li, X. Zheng, B. Zhou, M. Qi, and A. M. Weiner, "Microcomb-based true-time-delay network for microwave beamforming with arbitrary beam pattern control," *J. Lightwave Technol.* **36**(12), 2312–2321 (2018).
22. R. W. Boyd, *Nonlinear optics* (Academic Press, Amsterdam), 3rd ed.
23. A. Loayssa and F. J. Lahoz, "Broad-band RF photonic phase shifter based on stimulated Brillouin scattering and single-sideband modulation," *IEEE Photonics Technol. Lett.* **18**(1), 208–210 (2006).
24. K. Y. Song, M. G. Herráez, and L. Thévenaz, "Observation of pulse delaying and advancement in optical fibers using stimulated Brillouin scattering," *Opt. Express* **13**(1), 82–88 (2005).
25. Y. Okawachi, M. S. Bigelow, J. E. Sharping, Z. Zhu, A. Schweinsberg, D. J. Gauthier, R. W. Boyd, and A. L. Gaeta, "Tunable all-optical delays via Brillouin slow light in an optical fiber," *Phys. Rev. Lett.* **94**(15), 153902 (2005).

26. Z. Zhu, D. J. Gauthier, Y. Okawachi, J. E. Sharping, A. L. Gaeta, R. W. Boyd, and A. E. Willner, "Numerical study of all-optical slow-light delays via stimulated Brillouin scattering in an optical fiber," *J. Opt. Soc. Am. B* **22**(11), 2378–2384 (2005).
27. R. Pant, A. Byrnes, C. G. Poulton, E. Li, D.-Y. Choi, S. Madden, B. Luther-Davies, and B. J. Eggleton, "Photonic-chip-based tunable slow and fast light via stimulated Brillouin scattering," *Opt. Lett.* **37**(5), 969–971 (2012).
28. B. J. Eggleton, C. G. Poulton, P. T. Rakich, M. J. Steel, and G. Bahl, "Brillouin integrated photonics," *Nat. Photonics* **13**(10), 664–677 (2019).
29. R. Pant, C. G. Poulton, D.-Y. Choi, H. Mcfarlane, S. Hile, E. Li, L. Thevenaz, B. Luther-Davies, S. J. Madden, and B. J. Eggleton, "On-chip stimulated Brillouin scattering," *Opt. Express* **19**(9), 8285–8290 (2011).
30. S. Chin, L. Thévenaz, J. Sancho, S. Sales, J. Capmany, P. Berger, J. Bourderionnet, and D. Dolfi, "Broadband true time delay for microwave signal processing, using slow light based on stimulated Brillouin scattering in optical fibers," *Opt. Express* **18**(21), 22599–22613 (2010).
31. W. Li, N. H. Zhu, L. X. Wang, J. S. Wang, J. G. Liu, Y. Liu, X. Q. Qi, L. Xie, W. Chen, X. Wang, and W. Han, "True-time delay line with separate carrier tuning using dual-parallel mzm and stimulated Brillouin scattering-induced slow light," *Opt. Express* **19**(13), 12312–12324 (2011).
32. I. Aryanfar, D. Marpaung, A. Choudhary, Y. Liu, K. Vu, D.-Y. Choi, P. Ma, S. Madden, and B. J. Eggleton, "Chip-based Brillouin radio frequency photonic phase shifter and wideband time delay," *Opt. Lett.* **42**(7), 1313–1316 (2017).
33. M. Merklein, B. Stiller, and B. J. Eggleton, "Brillouin-based light storage and delay techniques," *J. Opt.* **20**(8), 083003 (2018).
34. G. P. Agrawal, "Chapter 9 - stimulated Brillouin scattering," in *Nonlinear Fiber Optics* (Fourth Edition), G. P. Agrawal, ed. (Academic Press, San Diego, 2006), Optics and Photonics, pp. 329–367, fourth edition ed.
35. M. B. Ayun, A. Schwarzbaum, S. Rosenberg, M. Pinchas, and S. Sternklar, "Photonic radio frequency phase-shift amplification by radio frequency interferometry," *Opt. Lett.* **40**(21), 4863–4866 (2015).
36. Y. Liu, A. Choudhary, D. Marpaung, and B. J. Eggleton, "Gigahertz optical tuning of an on-chip radio frequency photonic delay line," *Optica* **4**(4), 418–423 (2017).
37. L. McKay, M. Merklein, A. C. Bedoya, A. Choudhary, M. Jenkins, C. Middleton, A. Cramer, J. Devenport, A. Klee, R. DeSalvo, and B. J. Eggleton, "Brillouin-based phase shifter in a silicon waveguide," *Optica* **6**(7), 907–913 (2019).
38. L. McKay, M. Merklein, A. Choudhary, Y. Liu, M. Jenkins, C. Middleton, A. Cramer, A. Chilton, J. Devenport, K. Vu, D. Choi, P. Ma, S. J. Madden, R. DeSalvo, and B. J. Eggleton, "Broadband Brillouin phase shifter utilizing RF interference: Experimental demonstration and theoretical analysis," *J. Lightwave Technol.* **38**(14), 3624–3636 (2020).
39. W. Bogaerts, P. De Heyn, T. Van Vaerenbergh, K. De Vos, S. Kumar Selvaraja, T. Claes, P. Dumon, P. Bienstman, D. Van Thourhout, and R. Baets, "Silicon microring resonators," *Laser Photonics Rev.* **6**(1), 47–73 (2012).
40. Q. Chang, Q. Li, Z. Zhang, M. Qiu, T. Ye, and Y. Su, "A tunable broadband photonic RF phase shifter based on a silicon microring resonator," *IEEE Photonics Technol. Lett.* **21**(1), 60–62 (2009).
41. M. Pagani, D. Marpaung, and B. J. Eggleton, "Ultra-wideband microwave photonic phase shifter with configurable amplitude response," *Opt. Lett.* **39**(20), 5854–5857 (2014).
42. Y. Liu, A. Choudhary, G. Ren, K. Vu, B. Morrison, A. Casas-Bedoya, T. G. Nguyen, D.-Y. Choi, P. Ma, A. Mitchell, S. J. Madden, D. Marpaung, and B. J. Eggleton, "Integration of Brillouin and passive circuits for enhanced radio-frequency photonic filtering," *APL Photonics* **4**(10), 106103 (2019).
43. B. Morrison, A. Casas-Bedoya, G. Ren, K. Vu, Y. Liu, A. Zarifi, T. G. Nguyen, D.-Y. Choi, D. Marpaung, S. J. Madden, A. Mitchell, and B. J. Eggleton, "Compact Brillouin devices through hybrid integration on silicon," *Optica* **4**(8), 847–854 (2017).
44. X. Ji, F. A. S. Barbosa, S. P. Roberts, A. Dutt, J. Cardenas, Y. Okawachi, A. Bryant, A. L. Gaeta, and M. Lipson, "Ultra-low-loss on-chip resonators with sub-milliwatt parametric oscillation threshold," *Optica* **4**(6), 619–624 (2017).
45. J. F. Bauters, M. L. Davenport, M. J. R. Heck, J. K. Doylend, A. Chen, A. W. Fang, and J. E. Bowers, "Silicon on ultra-low-loss waveguide photonic integration platform," *Opt. Express* **21**(1), 544–555 (2013).
46. S. J. Madden, D.-Y. Choi, D. A. Bulla, A. V. Rode, B. Luther-Davies, V. Ta'eed, M. Pelusi, and B. Eggleton, "Long, low loss etched As<sub>2</sub>S<sub>3</sub> chalcogenide waveguides for all-optical signal regeneration," *Opt. Express* **15**(22), 14414–14421 (2007).
47. M. Tran, D. Huang, T. Komljenovic, J. Peters, A. Malik, and J. Bowers, "Ultra-low-loss silicon waveguides for heterogeneously integrated silicon/iii-v photonics," *Appl. Sci.* **8**(7), 1139 (2018).
48. R. V. Laer, B. Kuyken, D. V. Thourhout, and R. Baets, "Interaction between light and highly confined hypersound in a silicon photonic nanowire," *Nat. Photonics* **9**(3), 199–203 (2015).
49. E. A. Kittlaus, H. Shin, and P. T. Rakich, "Large Brillouin amplification in silicon," *Nat. Photonics* **10**(7), 463–467 (2016).
50. E. A. Kittlaus, N. T. Otterstrom, P. Kharel, S. Gertler, and P. T. Rakich, "Non-reciprocal interband Brillouin modulation," *Nat. Photonics* **12**(10), 613–619 (2018).